The Astrophysical Journal, 685:629–645, 2008 September 20

THE FILAMENT–MORETON WAVE INTERACTION OF 2006 DECEMBER 6

Holly R. Gilbert,[1] Antoun G. Daou,[1] Daniel Young,[1] Durgesh Tripathi,[2] and David Alexander[1]
Received 2008 February 4; accepted 2008 May 26

ABSTRACT

We utilize chromospheric observations obtained at MLSO of the 2006 December 6 Moreton wave, which exhibits two distinct fronts, and subsequent filament activation to conduct a comprehensive analysis of the wave-filament interaction. By determining the period, amplitude, and evolution of the oscillations in the activated filament, we make certain inferences regarding the physical properties of both the wave and the filament. The large-amplitude oscillations induced in the filament by the wave passage last on the order of 180 minutes and demonstrate a complicated mixture of transverse and perpendicular motion with respect to the filament spine. These oscillations are predominantly along the filament axis, with a period of ~29 minutes and maximum line-of-sight velocity amplitude of ~41 km s^{-1}. A careful examination of the complex oscillatory response of the filament elucidates some of the fundamental characteristics of the related Moreton wave. Specifically, we infer the maximum total kinetic energy involved in the interaction, the structure and topology of the passing wave, and discuss implications for the topology of the responding magnetic structure supporting the filament. The results of this observational study equip us with a better understanding of how filaments become activated and the nature of their responses to large propagating disturbances.

Subject headings: Sun: activity — Sun: chromosphere — Sun: coronal mass ejections (CMEs) — Sun: filaments

1. INTRODUCTION

Moreton waves, disturbances rapidly propagating across the solar surface in Hα observations, have been observed for decades. The range of speeds of the earliest Moreton waves detected is approximately 550–2500 km s^{-1} (Smith & Harvey 1971), with an average speed of about 1000 km s^{-1} (Moreton 1960; Athay & Moreton 1961; Smith & Harvey 1971). Although they are in general more easily detectable near the flare site where they originate, they can also be observed as far as 200,000 km away (Athay & Moreton 1961). More recently, chromospheric wavelike phenomena have also been observed in the He I (λ10830) data (hereafter referred to as He I) taken at the Mauna Loa Solar Observatory (MLSO). Waves observed in the He I data usually have a leading wave front traversing the visible solar disk that appears dark due to enhanced absorption of the background photospheric continuum (Vršnak et al. 2002; Gilbert et al. 2004b). Throughout the rest of this paper, we use the term "chromospheric wave" to describe wave phenomena in cotemporal Hα and He I observations. When referring to Hα observations independent of He I, we refer to wave phenomena as Moreton waves.

A similar phenomenon has been detected in the corona: coronal waves have been systematically observed with the EIT telescope (launched in December 1995), and are thus commonly labeled "EIT waves" (Thompson et al. 1999; we use the terms coronal waves and EIT waves interchangeably). If a relationship exists between EIT waves and Moreton waves, the nature of such a relationship is not well understood. In some previous studies Moreton waves have been found to be cospatial with EIT waves (Khan & Aurass 2002; Warmuth et al. 2001; Pohjolainen et al. 2001; Thompson et al. 2000). In another study completed by Eto et al. (2002), it was found that a Moreton wave and an EIT wave produced by a flare event are not cospatial and have very different velocities. The general description of EIT waves is consistent with that of Moreton waves, but properties such as average speed and distance traveled are notably different. EIT waves usually have a leading front observed in emission traveling between 200 and 600 km s^{-1} (Thompson et al. 1998, 1999) that can often be followed across the entire solar disk, although the speed of EIT waves can be as low as 50 km s^{-1} (Tripathi & Raouafi 2007). In addition, the propagation distance across which EIT waves can be followed is usually much larger than that for Moreton waves. Another very interesting and common characteristic of EIT wave propagation is its modification by the presence of magnetic solar features such as active regions and polarity boundaries (Thompson et al. 1999).

The determination of the spatial extent to which waves can travel (Athay & Moreton 1961) was due primarily to observations of abruptly disappearing or activated filaments, although the deflection of loops in active regions due to passing coronal waves has also been studied (Ofman & Thompson 2002). Distant filaments in the path of a traveling disturbance (600,000–700,000 km from the flare site—generally much farther than the observed wave front) sometimes undergo a temporary fading or disappearance in Hα, generally reappearing after only a minute. Some filaments also respond by oscillating back and forth without noticeably changing their appearance, as the wave propagates through. These large-amplitude oscillations (velocity ~20 km s^{-1}) are different from more commonly observed small-amplitude oscillations (velocity <2–3 km s^{-1}), which seem to be of a local nature and intrinsic to the filament itself. While much observational and theoretical work has been done on small-amplitude oscillations in filaments (Harvey 1969; Oliver et al. 1992, 1993; Engvold 2001; Oliver & Ballester 2002; Terradas et al. 2002), very little has been done on large-amplitude filament oscillations like the ones observed here. As a consequence, their physical nature is not yet fully understood. One proposed cause of large-scale oscillations is magnetic reconnection between a filament structure and nearby emerging magnetic flux (Isobe & Tripathi 2006; Isobe et al. 2007). Another cause of large-amplitude filament oscillations is the interaction with waves generated by flares or CMEs (Hyder 1966; Ramsey & Smith 1965; Eto et al. 2002; Okamoto et al. 2004);

[1] Department of Physics and Astronomy, Rice University, Houston, TX 77005; hgilbert@rice.edu, agdaou@rice.edu, dey3872@rice.edu, dalex@rice.edu.
[2] Department of Applied Mathematics and Theoretical Physics, University of Cambridge, Cambridge CB3 0WA, UK; D.Tripathi@damtp.cam.ac.uk.

however, the exact nature of the relationship between the properties of the wave (i.e., the speed, energy, and topology) and the filament activation is currently not well understood. Ramsey & Smith (1966) studied 11 oscillating filaments and found that each had its own characteristic frequency of oscillation, which was independent of the size of the flare, the distance from the flare, or the inferred wave velocity of the propagating disturbance. More recently, Eto et al. (2002) analyzed a filament oscillation which they propose was caused by a Moreton wave generated by a distant flare. Filament oscillations have also been attributed to coronal waves instead of chromospheric waves (e.g., Okamoto et al. 2004). Currently there is much speculation as to the exact relationship between coronal waves, chromospheric waves, and filament activations, and the nature of this relationship continues to be examined.

The large-scale chromospheric wave observed on 2006 December 6 (no corresponding EIT data is available, so we cannot study any associated coronal wave) has two characteristics generally associated with coronal waves: it is observed propagating across a large distance from its origin, and its leading front is easily detectable via a strong intensity signal. This unique event allows a careful analysis of a quiescent filament response to a passing chromospheric wave with two distinct fronts, leading to a better understanding of the nature of filament activation. Using Hα disk data and He I (λ10830) intensity and line-of-sight velocity data obtained at the MLSO, we obtain key information on the motion and velocities involved with the dynamic filament response. The following section contains a description of the MLSO data (the Appendix contains a detailed description of the algorithm applied to the He I data to obtain quantitative line-of-sight velocity). We present the results of our analysis in § 3, followed by a discussion of the conclusions and the implications of these results in the last section (§ 4).

2. DATA

The Hα and He I data used were obtained at the Mauna Loa Solar Observatory (MLSO) located on the big island of Hawaii. MLSO operates daily (weather permitting), collecting data for about 9 hr a day (typically 17:00–02:00 UT), producing some 170 images from each of its coronal instruments. The wave and filament activation for the event of 2006 December 6 were well observed by the Polarimeter for Inner Coronal Studies (PICS) Hα (λ6563) instrument and the Chromospheric Helium Imaging Photometer (CHIP), which observes in the He I (λ10830) spectral line. Both instruments operate with a 3 minute temporal cadence. The CHIP instrument (Elmore et al. 1998) observes in intensity and velocity (line-of-sight) at 2.3″ pixel^{-1} resolution using a filter configuration composed of seven filter positions. This configuration provides a measure of the line-of-sight component of velocity over the range of -90 to +90 km s^{-1}, with an accuracy of approximately ± 5 km s^{-1} (see Appendix for a detailed description of the algorithm used to obtain quantitative velocity information). The velocity data provided in the figures below is that currently provided by MLSO, offering qualitative information regarding flow away from or toward the observer. To extract quantitative velocity information, we have utilized the seven filter configuration of the CHIP instrument by applying a velocity algorithm (described in the Appendix) to localized regions of interest.

3. ANALYSIS

3.1. *Filament*

The quiescent filament of interest is located in the southern hemisphere at position angle (P.A.) $\sim 170^\circ$–190°, 0.8R, where R is the projected radial distance from image disk center, on 2006 December 6. Its axis is oriented very nearly parallel to the east-west direction, measuring approximately 0.02 $R_\odot$ in width and approximately 0.22 $R_\odot$ in length, where $R_\odot$ is one solar radius. Assuming that the filament rises uniformly with time, we roughly estimate its height at central meridian crossing to be 0.09 $R_\odot$ (the average of its height at the east limb $\sim$0.05 $R_\odot$ and at the west limb $\sim$0.12 $R_\odot$). The height of this filament may play an important role in its reaction to the passing wave (§ 3.3.). Prior to its dramatic activation, triggered by the chromospheric wave on 2006 December 6, this filament shows relatively little activity in the MLSO observations. Figure 1 shows the wave propagation in Hα (*top row*) and the initial stages of the filament activation in cotemporal Hα (*middle row*) and He I (λ10830) intensity (*bottom row*) data. There is a slight difference in filament appearance in the two lines at (Hα times) 18:57:33, 19:09:33, and 19:18:30 UT, marked by white circles in the figure. The filament disappearance in Hα represents what has historically been referred to as "winking," and occurs because at large velocities ($\sim$30–40 km s^{-1} for PICS, depending on how dark the original filament is), material will shift out of the narrow passband (0.5 Å for PICS). Line-of-sight velocity data provided by the CHIP telescope allows a detailed analysis of this winking filament's oscillations, and thus provides a better understanding of the phenomenon of disappearing and reappearing activated filaments.

Figure 2 shows the detailed evolution of the filament's velocity signal for over 2 hr following the initial activation, which begins at 18:52:06 UT, as downward motion becomes faintly evident in the velocity data at the eastern side of the filament. The white signature of downward motion (induced by compression of the imposing wave) propagates in the direction of the traveling wave, along the length of the filament, into the western portion. A rarefaction follows, as evidenced by signs of upward motion (dark in the velocity data) at 19:01:06 UT, and a subsequent propagation (also east to west) of this upward rebound. This type of oscillatory motion continues for almost 3 hr in the He I velocity data, in which a total of five obvious, complete oscillations (defined as the sequence of red-blue-red shifts) occur with a measured 18–39 minute period. Table 1 contains a list of several times at which a blue- and/or redshift is visible during several oscillations, with those chosen to determine the oscillatory period marked by an asterisk. Of particular interest is the combination of red- and blueshifts along the eastern portion of the spine first visible at 19:16:07 UT, and subsequently in many other images circled in Figure 2. This type of velocity signature indicates rotational motion if one considers a magnetic flux rope configuration with filament material flowing up one side, around the top of the rope, and falling downward along the other side. However, rotational motion would likely lead to a consistent velocity pattern (i.e., continual blueshift along a preferred side of the spine) visible in successive frames, which is absent. Instead, we interpret the velocity signatures in Figure 3 as an out-of-phase oscillation in which separate filament strands in the north side of the spine (recall the spine axis is oriented *predominantly* east-west) rebound from the initial downward compression before strands along the southern edge, illuminating the complex nature of the oscillatory motion.

To further investigate the north-south component of the oscillations, we examine the corresponding spatial displacement of the filament that is apparent in the velocity data (Fig. 4). The largest displacement of the spine in the direction perpendicular to its axis (i.e., north-south) occurs at 19:16:07 and 19:22:06 UT toward the north at 0.026 ($\pm$0.005) $R_\odot$, and at 19:40:07 UT toward the south at 0.019 ($\pm$0.005) $R_\odot$. The larger (apparent) displacement toward

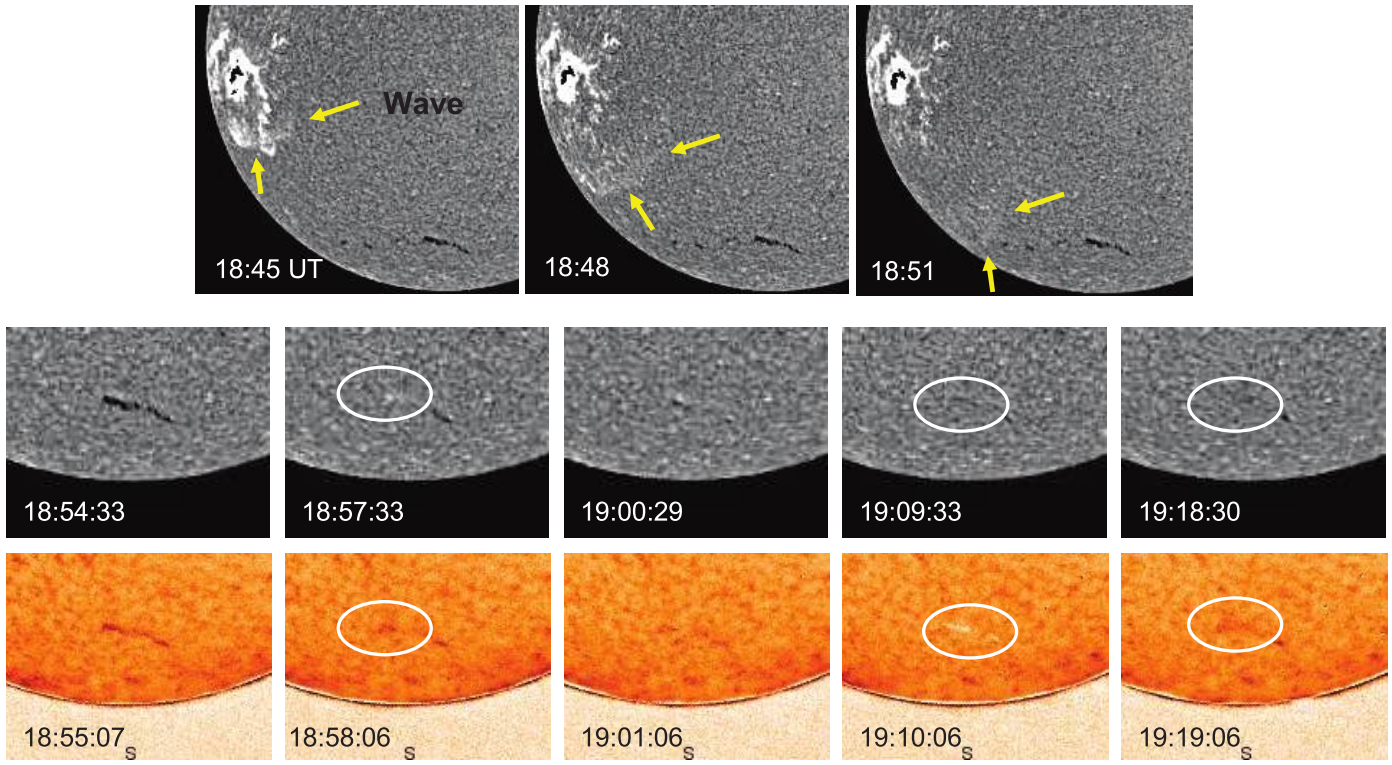

FIG. 1.—Wave observed in Hα data from MLSO (*top*), and the initial stages of filament response to the passing wave in Hα (*middle*) and He I (λ10830) intensity (*bottom*) data from MLSO. White circles show the largest differences in appearance in the filament in the two lines. At 19:10:06 UT the velocity toward the observer is large enough to significantly impact the mid-blue filter, yielding a blueshift (*white*) signal in the He I *intensity* data, a consequence of how the seven-filter configuration of the CHIP instrument is constructed (see Appendix).

the north may be a result of foreshortening, since the filament is located at a large distance from disk center in the south.

Following approximately 3 hr of oscillatory behavior, the filament relaxes back into a relatively stable state without erupting. It is remarkably similar in size and location, indicative of a complete recovery after its dramatic disturbance. The similar appearance in structure and location of the filament prior to and following activation, along with no evidence of an eruption in this region throughout the observing day, indicates that the propagating wave only caused a temporary disturbance, with no lasting effects on the magnetic structure supporting the filament mass.

3.2. *Chromospheric Wave*

The chromospheric wave responsible for the filament activation is visible in MLSO Hα (Fig. 1) and He I (λ10830) (intensity and velocity) data (Fig. 5) and has been studied in detail by K. S. Balasubramaniam et al. (in preparation). This spectacular wave is associated with a class X6.5 flare, also captured in the MLSO data. Details of the possible relation between the flare structure and wave are discussed below. Balasubramaniam et al. find the wave front propagates nonuniformly at a maximum speed of 1600 km s^{-1}, extending broadly to the south and somewhat to the north.

An interesting property of this wave is an associated signal in the line-of-sight velocity data. This Doppler information indicates a moving velocity pattern consisting of a downward motion of the upper chromosphere (white front) followed by an upward motion (dark front) (Fig. 5, *bottom panel*). The general spatial relation between the He I intensity and velocity wave fronts is illustrated in Figure 6, where we have traced the propagating wave fronts onto running-difference intensity images. More than one wave front is apparent in the difference images, consistent with results in Gilbert et al. (2004a), where multiple waves were observed in two chromospheric wave events. The secondary wave front is traced in blue in Figure 6, and although at least one other wave front is apparent (barely) in animations, it is difficult to trace its very diffuse signal on the still frames.

To explore the temporal variation of wave front width, we combine measurements of the leading edge and separator (i.e., the lagging end of the leading front) to obtain an average width for each wave front (He I intensity, He I velocity, and Hα) at various times (Table 2). Determining the wave front width also helps in understanding the nature of the filament oscillation, to be discussed in § 3.3.3. The fronts expand significantly throughout their evolution in all of the data sets, an expected characteristic of diffusive wave propagation. There is a noticeable difference between the average width of the velocity fronts and that of the intensity fronts, consistent with the picture presented in Gilbert et al. (2004a; see Fig. 10), which explains the He I *intensity* signature as the "imprint" of the overlying coronal wave and the *velocity* signature as a consequence of slow-mode waves, generated in the low corona by the edge of the coronal wave, and traveling downward through the transition region to impact the chromosphere, thereby producing the observed downward/upward pattern in the line-of-sight velocity. In this interpretation waves traveling through the transition region detach from their associated chromospheric and coronal fronts and rapidly become nearly horizontal. Only detached slow-mode waves traveling in a low-β plasma and propagating nearly parallel to the magnetic field are longitudinal and compressive, leading Gilbert et al. (2004a) and the present authors to propose that the velocity signal (compression followed by rarefaction) results from such secondary waves. The chromospheric area affected by the generated slow-mode waves appears to be smaller than the chromospheric "imprint" of the finite-width fast-mode pressure pulse propagating through the corona, which is consistent with the picture presented in Gilbert et al. (2004b, specifically the Appendix; 2004a).

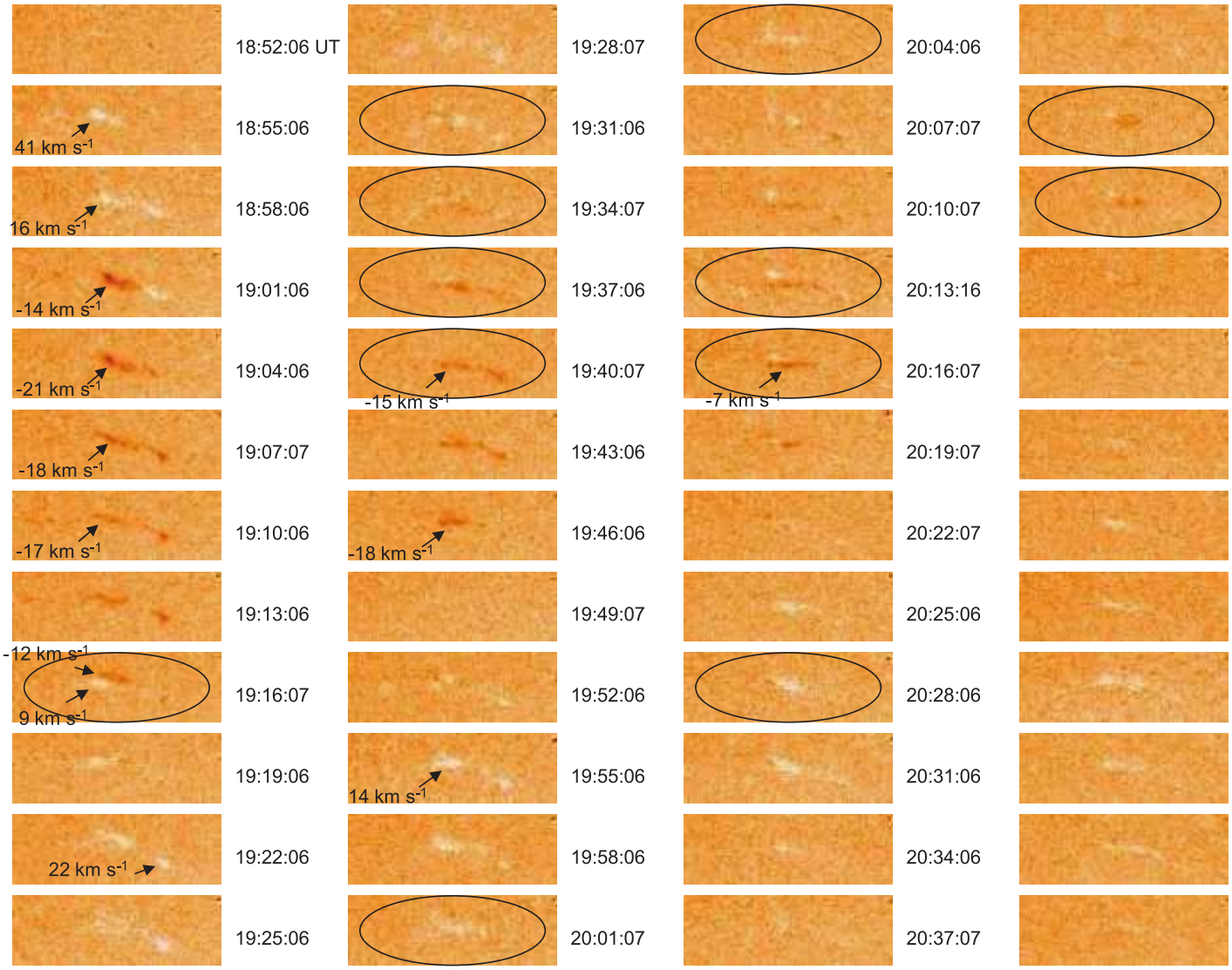

FIG. 2.—Filament region in a series of line-of-sight velocity images illustrating the detailed evolution of the dynamic filament response. Dark (white) indicates motion toward (away from) the observer; note the very faint redshift at the filament location in the velocity data at 18:52 UT. The black circles mark those images in which a complicated mixture of parallel and perpendicular (with respect to the filament axis) oscillations occur.

3.2.1. *Wave-Flare Relationship*

The primary focus of the present paper is on the nature of the interaction between the chromospheric wave and activated filament of 2006 December 6, but we provide here an auxiliary analysis of the possible relation between the structure and evolution of the flare and the existence of multiple wave fronts. A more thorough analysis of the flare and wave can be found in K. S. Balasubramaniam et al. (in preparation).

A large flare, recorded with an X6.5 magnitude in the *GOES* satellite soft X-ray energy classification, occurred in the same active region (AR 10930) as the apparent wave-front origins. The first sign of an observed wave front in the MLSO data occurs at 18:46:07 UT in CHIP (He I; Fig. 6) and 18:45:30 UT in PICS (Hα; Fig. 1) in a region covering a finite angular extent that encompasses the flare site. Given the limitation of the 3 minute cadence of the data, it is not possible to determine the exact location of the wave origin, and therefore whether it is generated by the flare or the corresponding CME (Gilbert et al. 2004a). However, we explore interesting flare-wave comparisons under the assumption that these waves were triggered by the dynamic flare process and that they are circularly propagating (the latter assumption is used only as a guide to allow extrapolation of the wave fronts). Based on the measured wave kinematics, we extrapolate the wave evolution backward, prior to its first observation, to see how the flare structure and evolution relate to the extrapolated spatial and temporal wave-front origins.

MLSO He I (λ10830) images are used to study the kinematics of the leading and secondary waves, both of which are measurable in four consecutive frames: from 18:46:07 to 18:55:07 UT (leading front) and from 18:49:07 to 18:58:06 UT (secondary front). We measure an average radial propagation speed for the first wave front of 1021 ± 52 km s^{-1} (after correcting for projection effects), and assume that this speed remains uniform along the whole wave front. Using this inferred wave speed, we extrapolate back to the flare source and estimate the trigger time of the first front as 18:41:08 ($\pm$36 s) UT. We perform a similar analysis of the secondary wave front, resulting in an average speed of 685 ± 59 km s^{-1} and corresponding extrapolated start time of 18:46:40 ($\pm$20 s) UT.

These extrapolated start times for the wave fronts have an interesting correlation with the complex flare evolution. The

TABLE 1
VISIBILITY OF RED- AND BLUESHIFTS

Time of Velocity Image (UT)	Eastern Filament	Western Filament
18:52:06	Red	...
18:58:06	Red*	Red
19:01:06	Strong blue	Strong red*
19:07:07	Blue	Blue
19:16:07	Red* + blue	...
19:31:06	Weak red + weak blue	Weak red*
19:34:07	Weak red + weak blue	Weak blue
19:37:06	Weak red + blue	Blue
19:43:06	Blue	Blue
19:52:06	Weak red*	Weak red*
20:01:07	Weak red + weak blue	Weak blue
20:13:16	Red + blue	Weak red* + weak blue
20:19:07	Blue	Weak red
20:25:06	Red*	...
20:40:07	Weak blue	...
20:55:06	Weak red*	...
21:19:07	Blue	...
21:34:07	Weak red*	...

NOTE.—Asterisks indicate shifts chosen to establish the oscillatory period.

impulsive phase and initiation of the flare is best examined using hard X-ray emission, as this provides insight into the spatial and temporal development of the early phase of energy release in the flare that might be linked to wave production. The *RHESSI* telescope (Lin et al. 2002) enables us to examine the flare hard X-ray emission with high spatial, spectral and temporal resolution. The *RHESSI* hard X-ray light curve (Fig. 7) shows that the flare comprises several hard X-ray bursts: the first and largest burst is recorded in the range 18:41:20–18:44:00 UT, with a peak around 18:42:30 UT, and a second large burst is recorded from 18:46:30–18:48:40 UT, with a peak around 18:47:20 UT. For comparison, the extrapolated start times of the two wave fronts are marked on Figure 7; both imply an origin coincident with the onset of the corresponding hard X-ray burst. Motivated by this potential temporal correlation between the two flare bursts and the wave start times, we include a search for a possible spatial correlation. Spectral images of the flare for the relevant times (covering the range of 25–100 keV) are generated using the PIXON algorithm (Metcalf et al. 1996) and used to compute the hard X-ray flux centroid. Figure 8 contains a plot of the centroids for individual emission locations in three different phases: the crosses denote the phase before the first burst (18:38:00–18:41:00), the asterisks represent the centroids during the first large burst (18:41:00–18:46:00), and the diamonds denote the phase during the second large burst (18:46:00–18:50:00). The extrapolated, circular wave-front origins are overlaid on the plotted hard X-ray emission (the leading front origin is located north of the secondary

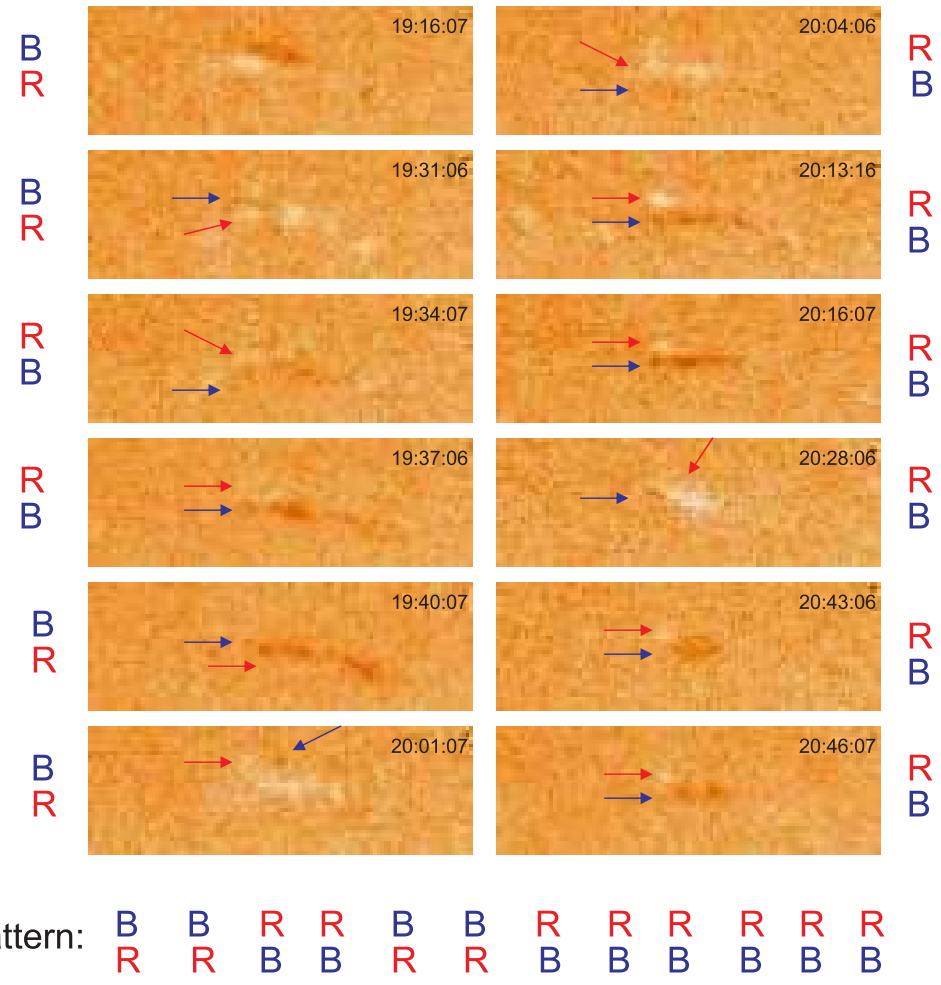

FIG. 3.—Line-of-sight velocity images in which the complicated oscillatory nature of the filament is apparent. The time between images showing a north-south pattern of blue- and redshifts varies, and the overall change in the pattern (inconsistent with rotational motion) is also shown.

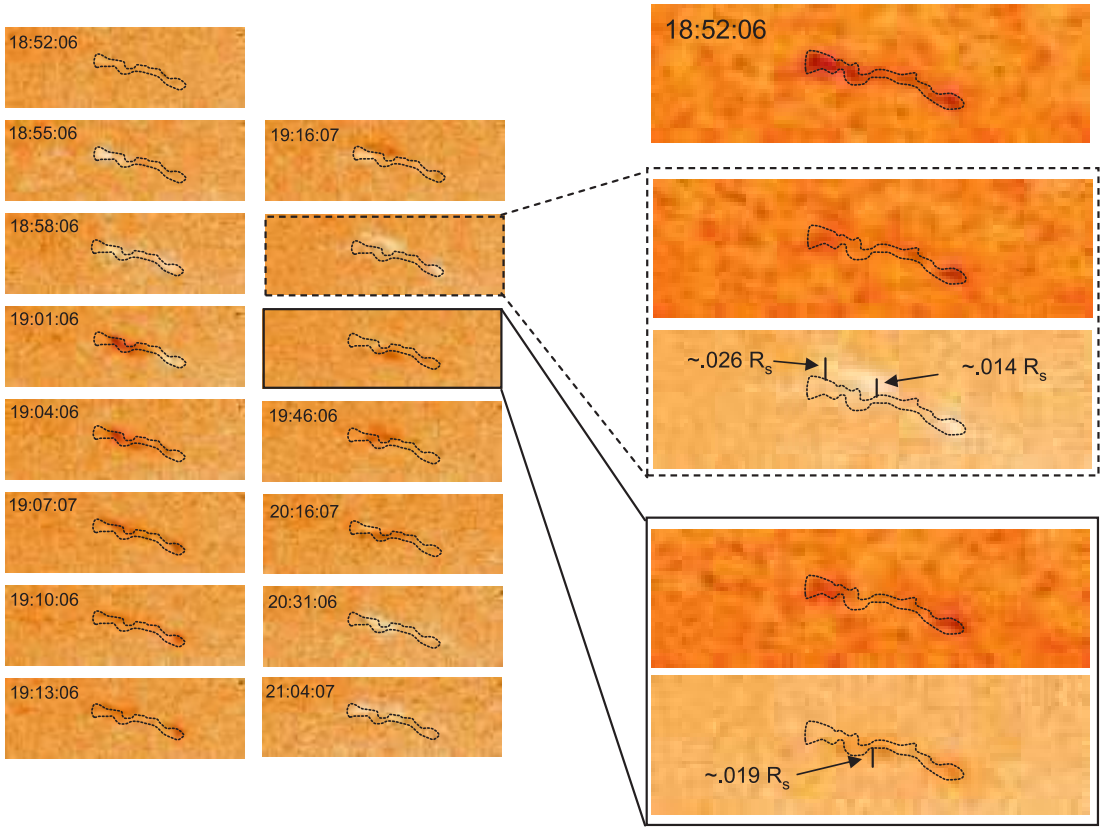

FIG. 4.—Series of line-of-sight velocity images showing the spatial displacement of the filament with respect to its location just prior to activation. Its initial location (18:49:06 UT) in the He I intensity data (*top right box*) is overlaid on the velocity images as the traced dotted line, and subsequently used to measure its north-south displacement ($\pm 0.005\ R_\odot$) at 19:22 and 19:40 UT.

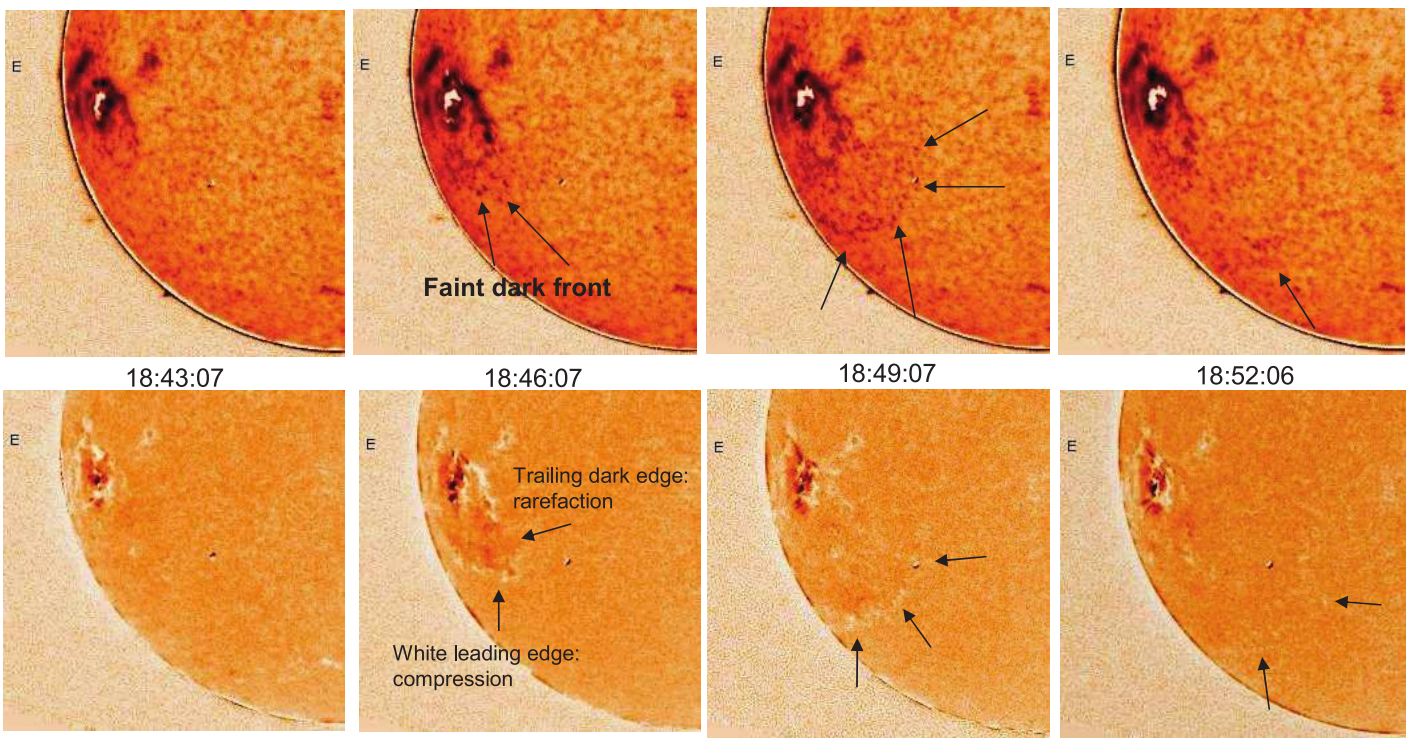

FIG. 5.—Wave observed in cotemporal He I (λ10830) intensity (*top*) and line-of-sight velocity (*bottom*) data. Black arrows mark the leading edge of the wave front in both data sets.

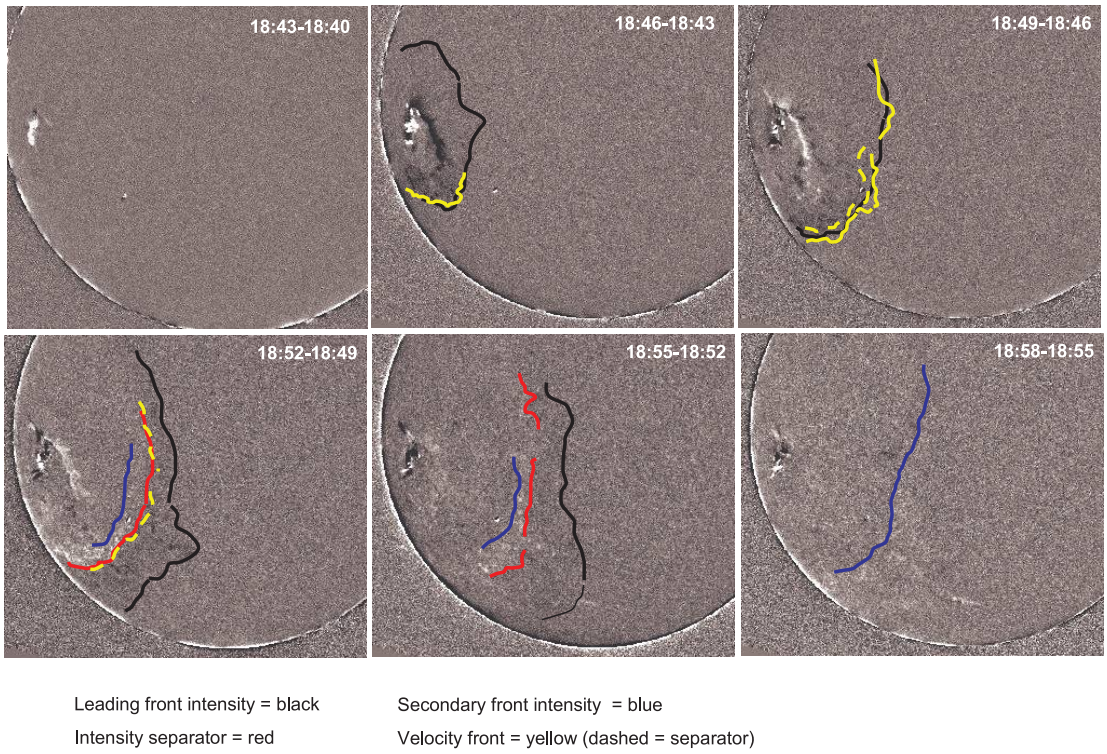

FIG. 6.—Propagating wave fronts traced on running-differenced He I intensity images. Black lines represent the leading edge of the intensity front, and solid yellow lines represent the nearly cotemporal leading edge of the velocity front. We define a separator as the trailing edge of the wave front, which separates the light from the dark (or the dark from the light) in running-differenced images. Red lines represent the intensity "separators," and the velocity "separators" are marked by dashed yellow lines. Blue lines mark a secondary wave front.

one). This plot is suggestive of a possible spatial correlation between the inferred birth regions of both waves and the two large hard X-ray bursts. In particular, we note that the asterisks in Figure 8, representing the first large burst, are located within the inferred circular area of the first wave-front origin. The inferred secondary wave-front origin corresponds to the southern diamonds on the plot, which represent the phase during the second large burst in the flare. The diamonds located to the north are a minor source of emission with respect to those located in the south of the figure (A. G. Daou et al., in preparation). These spatial and temporal correlations, although containing high uncertainties and resulting from various assumptions about the wave evolution, provide a tantalizing glimpse into the possible flare–multiple wave relationship.

3.3. *Wave-Filament Relation*

A careful analysis of the filament activation and the wave allow us to examine the relationship between the two. We begin by exploring simple observational properties of the interaction, e.g., the temporal correlation and the inference of wave speed using filament observations, before delving into more complicated physical properties, e.g., total kinetic energy in the interaction and possible restoring forces.

TABLE 2
AVERAGE WAVE FRONT WIDTHS

TIME OF He I INTENSITY (Hα) (UT)	AVERAGE WAVE FRONT WIDTH (± 0.01) ($R_\odot$)		
	He I Intensity	Hα	He I Velocity for Red/Blueshifts
18:46:07 (18:45:30)	0.14	0.08	0.02 (R) / 0.03 (B)
18:49:07 (18:48:33)	0.16	0.13	0.04 (R) / Faint (B)
18:52:06 (18:51:33)	0.29	0.26	Too faint in R and B

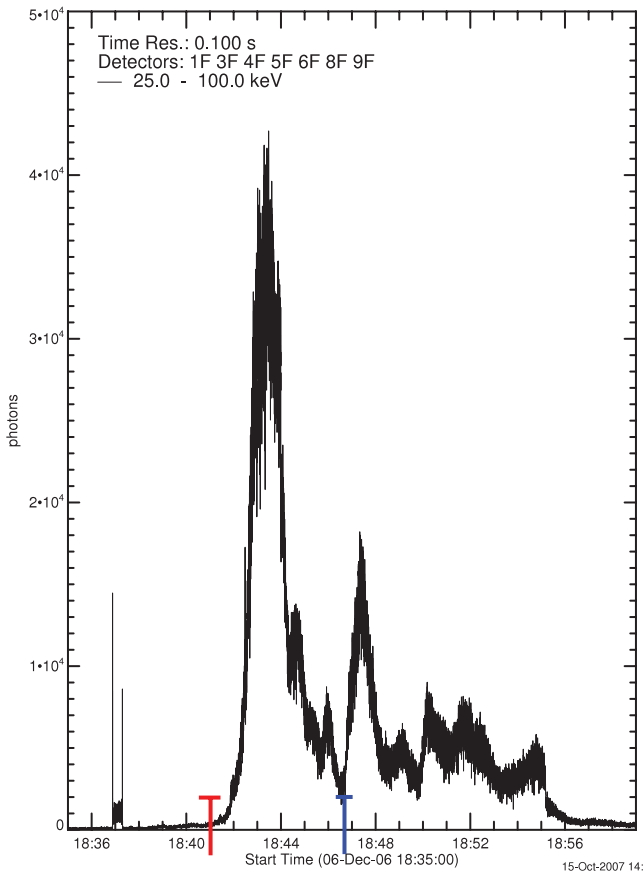

FIG. 7.—*RHESSI* hard X-ray light curve with the extrapolated start times of the two wave fronts marked on the temporal axis.

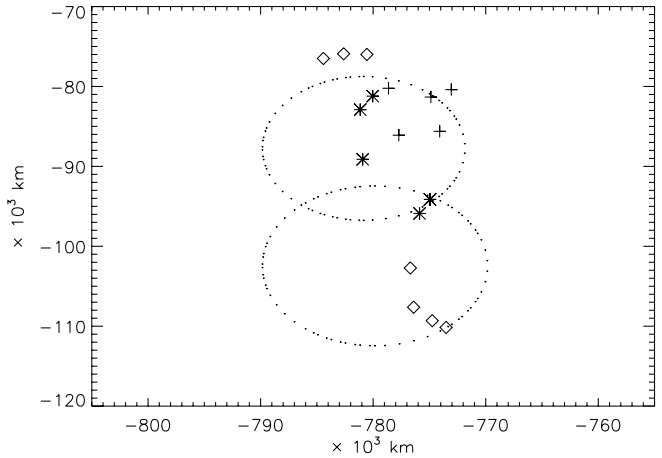

FIG. 8.—Plot of the centroids for individual emission locations in three phases: prior to first burst (*crosses*), during first large burst (*asterisks*), and during the second large burst (*diamonds*). The extrapolated, circular wave front origins are overlaid on the plotted emission centroids.

3.3.1. *Temporal and Spatial Relationship*

The temporal and spatial relationship between the leading edge of the wave front and the first signs of filament activation is illustrated in Figure 9. A very small velocity signal is apparent in the filament at 18:52:06 UT (*circled in the top panel*), inconsistent with the apparent location of the wave front in the differenced velocity and intensity data (*bottom panel*) if we assume that the contact between the wave front and the filament produces the velocity signature. A close examination of the differenced He I intensity data shows a broad, complicated leading wave front (Fig. 9, *bottom panel*) extending relatively close to the filament region. However, the complexity and spreading of the southward traveling wave front at 18:52:06 UT is not sufficient to explain the filament response. The small velocity signal visible in the eastern portion of the filament at this time indicates that the wave front extends farther than is visible in the intensity differenced images. This result is consistent with the picture of the wave as a traveling pressure pulse: the visible front reflects the region of the pressure pulse that is the most intense, but the pressure at the very front of the pulse, which is capable of interacting with the filament, may be too weak to detect in observations. A filament oscillation studied by Eto et al. (2002) has a similar premature activation with respect to its associated EIT wave front. Instead of applying the picture presented above to the EIT wave front, Eto proposed that the filament oscillation was caused by an "invisible" Moreton wave, or simply the visible Moreton wave projected to a distance where it is no longer detectable. Our interpretation of the interesting temporal discrepancy in the 2006 December 6 event may also apply to other filament activations, such as that presented in Eto et al.

3.3.2. *Wave Speed Inference*

The wave fronts are too diffuse to measure by the time they reach the filament, but we can infer the chromospheric wave speed by studying the filament response. Using velocity images at 18:55:07 and 18:58:06 UT, we measure the speed at which the line-of-sight downward velocity signal itself propagates along the axis of the filament spine, reflecting how quickly the wave passes through the filament, to be at least 619 km s^{-1}. This is a lower limit to the wave speed, because at 18:58:06 UT the entire length of the filament is visibly compressed downward, making it impossible to determine how far beyond the western end of the filament the wave has traveled (the wave front is no longer visible at this distance from its origin). Inferring a lower limit to the wave speed at the location of the filament is useful in the following analysis.

3.3.3. *Nature of the Filament Recovery*

Once the wave impacts the filament, we expect the filament to oscillate with some characteristic period in response to the initial wave-induced displacement, but the nature of the filament recovery from this displacement depends on the width of the initial wave front, the wave velocity, the topology of the wave front, the

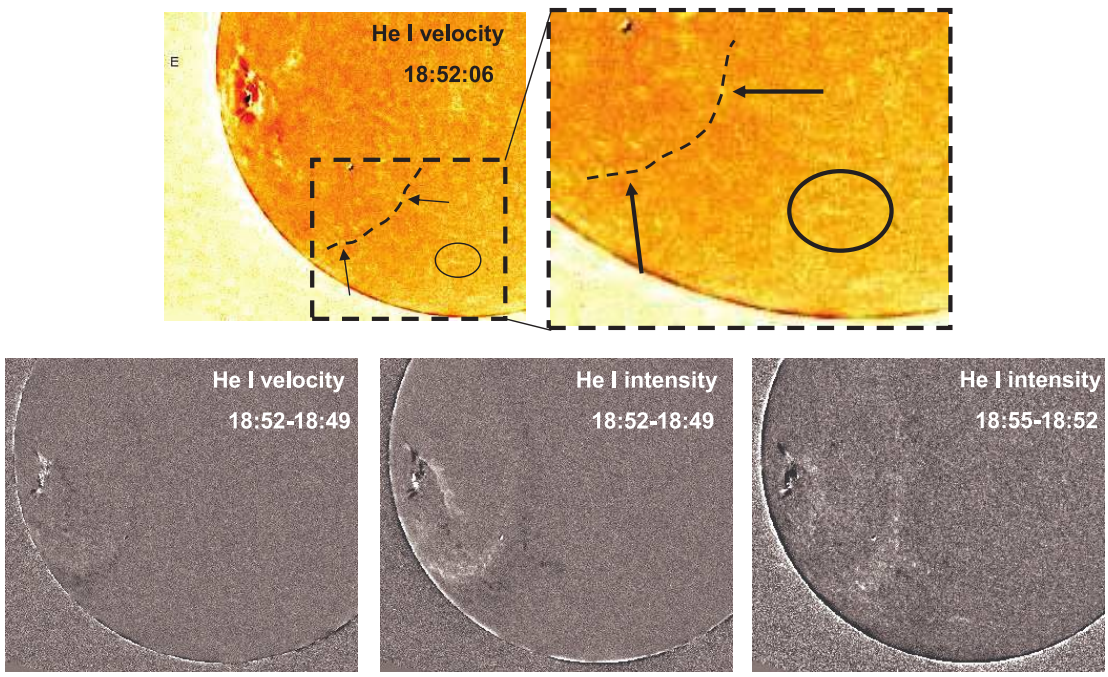

FIG. 9.—Leading wave front in He I velocity (*top*), and running-differenced He I velocity and intensity images (*middle*) at 18:52 UT 18:55 UT. The black arrows mark the location of the diffuse front, and the black circles show the region where the filament is located and its faint signature in the velocity data.

topology of the magnetic structure supporting the filament, and the mass of the filament. Although we do not know the mass of the filament or the topology of its supporting magnetic structure, the measurements of the wave front width and velocity can yield insight into the nature of the filament's recovery from being perturbed.

We expect the width of the wave front and the existence of multiple wave fronts to have an effect on the length of the recovery time for the oscillating filament. Although we do not know the restoring force of the filament (discussed in the following section), we can make some general inferences as to how quickly a filament bounces back from its initial displacement. For an infinitesimally small wave front traveling parallel to a filament axis, we expect each filament slice (i.e., cross section of the spine) to rebound relatively quickly following the passage of the front (on the order of seconds). Correspondingly, for a front of finite width, the amount of time it takes for the filament to bounce back will depend on the width of the passing front. We use our results to test this possibility by assuming our filament length of ~150,000 km, a wave front width of 0.29 $R_\odot$ (~201,550 km, the measured width of our front as it approaches the filament), and two different coherent wave-front speeds: 650 km s^{-1} (similar to the lower limit found in the filament region in § 3.3.2) and 1000 km s^{-1} (slightly slower than that measured closer to the flare). Given this assumed slow (fast) speed, the leading edge, which can be thought of as an infinitesimal front, will pass through the entire length of the filament spine in ~3.9 (~2.5) minutes, with the trailing edge delayed by ~5.2 (3.6) minutes (the time it takes just to reach the front of the filament). Therefore, we expect the eastern side of the filament to be exposed to constant compression (by the *visible* wave front) for approximately 5.2 (3.6) minutes in this simple picture. The time range between the first initial impact (18:52:06 $< t <$ 18:55:06 UT) and the first signs of rebounding (18:58:07 $< t <$ 19:01:06 UT) is 3–9 minutes, which is consistent with our calculated 5.2 (3.6) minutes of constant compression on the eastern side.

Just as we expect a wide wave front to delay a filament from bouncing back, a secondary wave might also affect the recovery time of the filament. Although the secondary wave front in Figure 6 is too faint to measure as it closely approaches the filament, we can estimate its time of arrival based on its velocity. Assuming it continues to travel at 685 km s^{-1} (§ 3.2) as it reaches the eastern portion of the filament, the secondary wave front arrival time is estimated to be ~19:05 UT. The filament compression caused by the secondary wave front, although perhaps not as intense as that caused by the first wave front, will either augment the original compression or delay the rebounding motion, depending on which direction the filament mass is traveling on impact. At 19:05 UT, our filament is completely blueshifted, and its maximum blueshifted velocity of -21 km s^{-1} is measured just prior at 19:04:06 UT. The arrival of the secondary wave may have retarded the blueshift in this case, but higher temporal resolution is required to fully understand how secondary wave fronts influence filament activation.

3.3.4. *Total Kinetic Energy*

The unique line-of-sight velocity information on the filament oscillations allows us to infer the total maximum kinetic energy involved with the wave-filament interaction. The maximum kinetic energy is equal to the work done by the pressure gradient force in the wave as it accelerates filament material, and can be found by estimating the filament mass and using the line-of-sight velocities in the filament activation. We use the average mass of quiescent filaments found in Gilbert et al. (2006) of 4×10^{14} g, and the maximum line-of-sight filament velocities of 41 km s^{-1} (redshift at 18:55:06 UT) and -21 km s^{-1} (blueshift at 19:04:06) to estimate the maximum kinetic energy:

$$\mathrm{KE_{red}} = \tfrac{1}{2}mv^2 = \tfrac{1}{2}\left(4\times10^{11}\ \mathrm{kg}\right)\left(41000\ \mathrm{m\ s^{-1}}\right)^2 = 3.36^{+0.87}_{-0.77}\times10^{20}\ \mathrm{J},$$

$$\mathrm{KE_{blue}} = \tfrac{1}{2}mv^2 = \tfrac{1}{2}\left(4\times10^{11}\ \mathrm{kg}\right)\left(21000\ \mathrm{m\ s^{-1}}\right)^2 = 8.82^{+4.68}_{-3.70}\times10^{19}\ \mathrm{J}.$$

These results provide an empirical inference of the total kinetic energy involved in a wave-filament interaction, consistent with the predicted energy required to induce quiescent prominence oscillations given by Kleczek & Kuperus (1969), ~10^{19}–10^{20} J.

3.4. *Other Wave-Induced Filament Activations*

An interesting aspect of the 2006 December 6 Moreton wave is the large spatial extent to which it propagates, resulting in the activation of two filaments. We utilize these concurrent events to briefly investigate the difference in filament responses to the same passing wave. To augment this investigation and gain insight into which filament or wave properties play a role in how dramatically filaments react to passing waves, we include an additional filament activation occurring on 2006 April 17.

3.4.1. *Northern Filament*

The Moreton wave on 2006 December 6 is most clearly visible traversing the solar disk toward the south, but it also propagates northward, activating a filament located close to the east limb in the northern hemisphere at ~P.A. 50°–60°, 0.85–0.95 R (where R is the projected radial distance from image disk center). The response of the northern filament (Fig. 10*a*) is much less dynamic than the southern filament, despite its relatively close proximity to the wave origin. The northern filament exhibits only two oscillations in the velocity data, compared to the five clearly observable oscillations of the southern filament, but if we consider the close proximity of the wave origin and the northern filament to the solar limb, we surmise that it is predominantly oscillating in the plane of the sky, creating difficulty in oscillatory detection in the line-of-sight velocity He I data. The northern filament, which first becomes activated at 18:52 UT, regains a stable structure after 19:09 UT, whereas the southern filament settles into a stable configuration after 20:39 UT. The large difference in the duration of the oscillations (i.e., 17 minutes for the northern filament compared to ~180 minutes for the southern filament) may be partly due to our line of sight, but it may also be due to the relative orientation of the filament axis with respect to the wave propagation direction. The perpendicular oscillations predominant in the northern filament, but relatively lacking in the southern filament, decay much more rapidly because they affect the ambient corona more than motions along the filament axis (Vršnak el al. 2007) (damping and restoring forces are addressed in § 4 below). By comparing these two filament responses induced by the same Moreton wave, we conclude that the strength of response is highly correlated with the intensity of the wave, and less dependent on the distance of the responding filament to the wave origin. The southward component of the wave is clearly more intense than the northward component, which may be a consequence of the amount of active region it must travel through near its origin. The discrepancy in intensity may also be related to the structure and evolution of the associated flare, which demonstrates an interesting north-south orientation (§ 3.2.). Whatever the cause of the differing wave front strengths in the

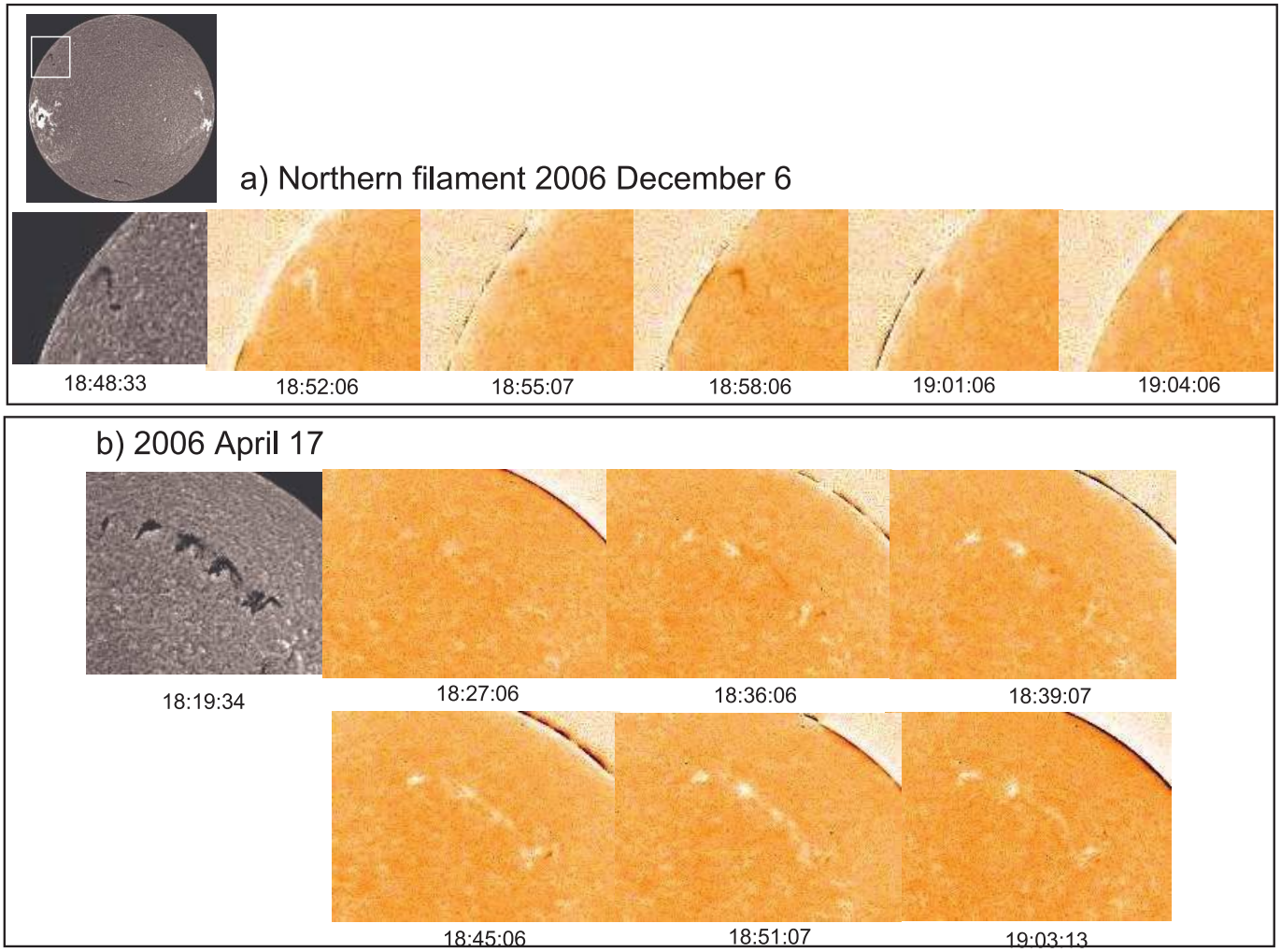

FIG. 10.—Northern filament activation on 2006 December 6 (*top*), and another filament activation caused by a coronal wave on 2006 April 17 showing similar oscillatory motion (*bottom*).

north and south directions, the difference in the associated filament responses indicates that there is a correlation with wave intensity.

Theories regarding the relationship between Moreton waves observed in Hα, chromospheric waves observed in He I (λ10830), and coronal waves observed in EIT can be found in many papers (Uchida 1968, 1970; Thompson et al. 2000; Warmuth et al. 2001; Eto et al. 2002; Vršnak et al. 2002; Okamoto et al. 2004; Gilbert et al. 2004b; Chen et al. 2005; Balasubramaniam et al. 2007), many of which assume that chromospheric waves have a coronal origin. Under that assumption, the height at which a filament is located in the atmosphere may be a key factor in how strongly it responds to a passing wave. Picturing our filament systems, with their surrounding magnetic fields and coronal plasma, as weight-loaded oscillators, we compare the lower lying filament system in the north to a stiffer spring (low-lying filaments often reside in active regions [Low 1996] or regions of strong magnetic fields), resulting in a shorter period and smaller velocity amplitude than a higher lying filament (a less stiff spring), when both are subjected to the same perturbation. To explore this possibility, we

TABLE 3
FILAMENT AND WAVE CHARACTERISTICS FOR THREE EVENTS

Characteristic	2006 Dec 6 Southern	2006 Dec 6 Northern	2006 Apr 17 Polar Crown
Magnitude of filament response	Strong	Weak	Medium
Number of filament oscillations (plane-of-sky)	5+	2	2–3
Duration of filament oscillatory motion (minutes)	~160+	~24	~90
Filament distance from flare ($R_\odot$)	~1.03	~0.59	~0.34
Maximum filament height ($R_\odot$)[a]	0.12	< 0.01	0.15
Intensity of wave[a]	Strong	Weak	Very weak
Speed of wave (km s^{-1})	~1000	~1000	Not measurable

[a] Characteristic likely to have an effect on how dramatically a filament responds to a passing wave.

compare the height of both activated filaments on 2006 December 6: the northern (less activated) filament resides very close to the surface ($<0.01\ R_\odot$), while the southern filament sits at approximately $0.09\ R_\odot$. We conclude that filament height plays a partial role in the nature of its response to passing waves.

3.4.2. *2006 April 17*

A large polar-crown filament became activated by a diffuse coronal wave traveling predominantly parallel to its axis on 2006 April 17 (Fig. 10*b*). There are a couple of major differences between this activation and those occurring on 2006 December 6. First, the 2006 April 17 wave is very weak, as it is not detectable in Hα, and only barely visible in EIT Fe XII (λ195) running differenced images. Second, the corresponding activated filament is very large and tall compared to the other filaments discussed in this paper, between 0.08 and 0.15 $R_\odot$ in height. Like the 2006 December 6 filament activations, the response of this filament is obvious in both MLSO Hα and He I (λ10830) intensity and velocity data. We observe three oscillations in this large, polar-crown filament, each lasting a relatively long time. Table 3 summarizes characteristics of the three filaments and their corresponding waves studied in the present paper. Based on this table, we suspect that both the intensity of the wave (whether it is coronal or chromospheric) and the height at which a filament is located in the atmosphere play a role in the extremity with which a filament responds to globally propagating waves.

4. DISCUSSION

Chromospheric observations of the 2006 December 6 Moreton wave and subsequent filament activations obtained at MLSO provide a rare opportunity to carefully analyze the wave-filament interaction. By analyzing the dramatic, complicated response of the southern filament to the passing wave, we infer physical properties of both the wave and the filament. First, we address the crucial insight into the filament properties obtained in this study, including (1) its complex oscillatory motion, (2) its oscillation properties (period and amplitude) (3) restoring forces, and (4) the resilience of the supporting magnetic system.

The velocity signature produced by the filament activation exhibits a complex oscillatory motion, in which separate strands of the filament oscillate slightly out of phase, producing a Doppler pattern similar to that exhibited by a rotating mass in a flux rope configuration. This type of filament response in the line-of-sight velocity data allows an analysis of the wave-filament interaction as a driven harmonic oscillator, with the observed oscillations characterized by a period of $\sim$22 minutes in the western portion and $\sim$31 minutes in the eastern portion (where there is a convolution of red- and blueshifts), velocity amplitude of 41 km s^{-1}, and oscillation duration of $\sim$180 minutes. While most large-amplitude filament oscillations caused by waves occur perpendicular to the prominence axis (Vršnak et al. 2007), the filament studied here exhibits complex oscillations that are aligned predominantly parallel to the axis, with a slight perpendicular component. The restoring force in a perpendicular oscillation can be explained in terms of magnetic tension (Hyder 1966; Kleczek & Kuperus 1969; Vršnak 1984, 1990). For motions along the local magnetic field, radiative damping has commonly been considered (Kleczek & Kuperus 1969; Terradas et al. 2001). This type of damping can be attributed to energy loss by emission of waves into the ambient corona (i.e., the oscillation of a filament generates a compressional wave in the surrounding corona, which reacts on the filament to dissipate the oscillatory power). Attributing most of the damping in our filament to the radiative processes, our long duration time of $\sim$180 minutes is consistent with radiative damping in the case where the medium surrounding the filament is of a coronal temperature (see Antiochos et al. 2000; a much shorter damping timescale would result if the oscillation is entirely inside a chromospheric medium, Jing et al. 2003). Moreover, the shorter damping time of the northern filament, with its axis aligned perpendicular to the wave, is consistent with a restoring force dominated by magnetic tension. Although we cannot say conclusively what the restoring force is in our event, we can infer the strength of the effective magnetic field that plays a crucial role (if it is of a magnetic origin) by considering the model of Kleczek & Kuperus (1969). According to this model, the period of the horizontal oscillation of a filament is given by

$$P = 4\pi LB^{-1}\sqrt{\pi\rho},$$

where $2L$ is the length of the filament, ρ is the mass density, and B is the strength of the magnetic field. Assuming $\rho = 10^{-13}$ g cm^{-1}, and using our measured values for $L = 7.49 \times 10^9$ cm, and $P =$ 1740 s (the average period), we infer $B \sim 30$ G. A similar analysis was done for the oscillating polar crown filament studied by Isobe & Tripathi (2006), who found $B = 9.8$ G. Our larger inferred field strength is consistent with the relatively smaller size and height of our filament. The discrepancy may also partly be due to the difference in the nature of the oscillations in these two events: Isobe & Tripathi proposed that their oscillations were triggered by the emerging flux below the erupting filament, as opposed to a globally propagating wave.

In the present analysis, the basic parameters of the filament oscillations, inferences of total kinetic energy, and magnetic field strength are important in the context of a particular filament model. Equally important in this context is the resilience of the magnetic system containing the filament mass, evidenced by the lack of eruption and lack of significant mass loss as a result of draining to the surface following the very dramatic filament activation. Both of these observations may have interesting implications for the topology of the supporting magnetic structure, as well as the topology and strength of the overlying arcades (e.g., Vršnak 1990). This type of observational study provides important constraints for existing filament models, and we hope will stimulate theorists to explore the interaction between filaments and chromospheric and coronal waves in existing and future models.

A careful examination of the filament response provides insight into some of the driving wave properties, since the nature of the response partly depends on wave-front topology and structure. In summary, our interpretation elucidates three interesting wave properties. First, the spatial and temporal inconsistency between the first observation of the filament response and the leading wave front suggests that the visible wave front is part of a larger, extended pressure pulse. Second, the slight delay in the filament rebound accompanying the initial compression supports the idea that the activated filament is sensitive to the width of the leading wave front, as well as to the presence of less intense trailing wave fronts. Finally, the relatively large He I line-of-sight velocities observed at the time of the initial filament activation point to a slightly forward-inclined (with respect to the surface and in the direction of its propagation) wave-front topology. Vršnak et al. (2002) also conjecture that wave fronts are inclined in their interpretation of how He I waves are related to Moreton waves observed in Hα.

Understanding the relationship between various solar phenomena continues to be a driving goal in solar physics. Observational studies such as that conducted here provide a better understanding

of the interaction between global waves and CMEs, flares, and distant surface features such as quiescent filaments, placing constraints on models of the initiation and evolution of such phenomena. The unprecedented spatial and temporal resolution of new data provided by such spacecraft as *STEREO* and *Hinode* will further our ability to study the wave-filament interaction, advancing our overall knowledge of solar eruptive behavior.

We would like to thank Thomas Holzer for his insightful comments and help in developing an appropriate velocity algorithm. We also thank Giuliana deToma and Joan Burkepile at the High Altitude Observatory for providing the MLSO data and helping with the interpretation. D. Tripathi thanks STFC for support. This work was partially supported by NASA grants NNX07AI10G and NNG04GO68G.

APPENDIX A

The Chromospheric Helium Imaging Photometer (CHIP) at MLSO obtains observations in the spectral region surrounding the He I (λ10830) line. To understand the details of the seven-filter CHIP configuration and velocity algorithm used in this study, it is important to first consider the shape of the He I line. We utilize spectral scans of the 10830 Å line for different types of features on the solar disk provided by Harvey & Livingston (1994). Figure 11 shows six such scans, corresponding to bright features (curves *a* and *c*), a typical network element (curve *d*), and filaments and plages (curves *e*, *g*, and *h*). Accounting for the characteristics noted in the figure caption, we have used synthetic spectra created by fitting the six line profiles from Figure 11 and the other solar and terrestrial absorption lines observed in this spectral region, which are subsequently used to study the effect of Doppler shifts on the CHIP observations of these various types of features. (Our approach is based on a suggestion by T. E. Holzer 2006, private communication.) For relatively dry atmospheric conditions, the fit (i.e., the synthetic spectrum) for curve *g* (appropriate for filaments) of Harvey & Livingston, along with the fits for the other solar and terrestrial lines in the 10830 Å region and the CHIP filter configuration, are shown in Figure 12 with seven filter positions: line-center position (O), three blue positions (B1, B2, and B3), and three red positions (R1, R2, and R3). In the CHIP intensity and line-of-sight velocity observing configuration, a tunable Lyot filter is sequentially positioned at the seven wavelength locations. At present, the CHIP velocity data is produced by subtracting the inner red (R1) filter from the inner blue (B1) filter, the output of which is shown in the velocity figures throughout this paper. These velocity images are only qualitative, since the line-of-sight velocity information provided is little more than a qualitative indication that flow is toward or away from the observer at a speed of a few to a few tens of km s^{-1}. To obtain quantitative velocity information, we have applied an algorithm (discussed below) to a relatively small region (where the filament resides) showing a strong He I signal.

The CHIP intensity data is obtained with the current seven-filter configuration in the following way. The mid-blue (B2) filter is treated as the continuum filter, in the sense that the line intensity is determined by the filter subtraction O−B2. Therefore, when the velocity toward the observer is large enough to impact the mid-blue filter, a blueshift (i.e., white) will appear in the *intensity* data. This phenomenon can be detected in the present study at 19:04–19:10 UT in the filament region, corresponding to a large blueshift at these times. Since the qualitative velocity data alone may be deceiving (e.g., a blueshift may disappear even with strong upflow), we utilize the intensity data in conjunction with the qualitative velocity data to determine whether a strong upflow (indicated by a white signal in the intensity data) is occurring. We note that there is no corresponding qualitative "guide" with redshifts, or downflow, and the only way to determine whether downflow is increasing or decreasing is to perform some equivalent of the analysis discussed below.

To obtain quantitative line-of-sight velocity information using the seven-filter configuration, we have normalized the output from each of the seven filters, so that the normalized output reflects only the photospheric continuum radiation and the He I (λ10830) absorption line. We then used these normalized intensities measured at the seven different filter positions to infer the line-of-sight velocity of the structure being observed.

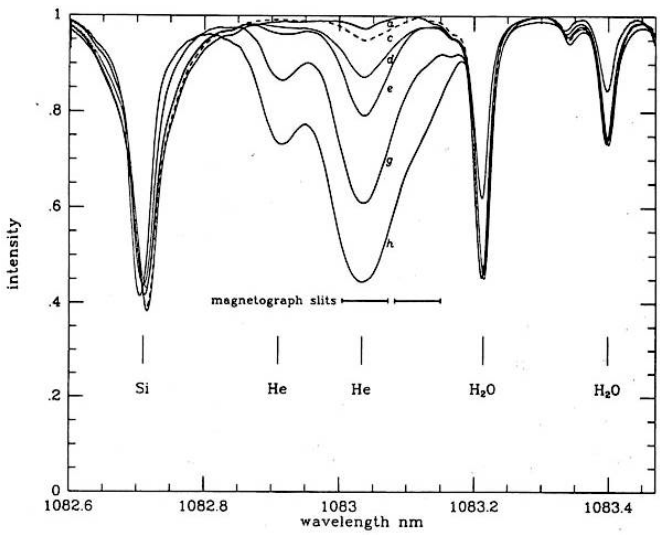

FIG. 11.—Spectral scans of the 1083 nm region from Harvey & Livingston (1994). The scans correspond to bright features (*a* and *c*), a typical network element (*d*), and filaments and plages (*e*, *g*, and *h*).

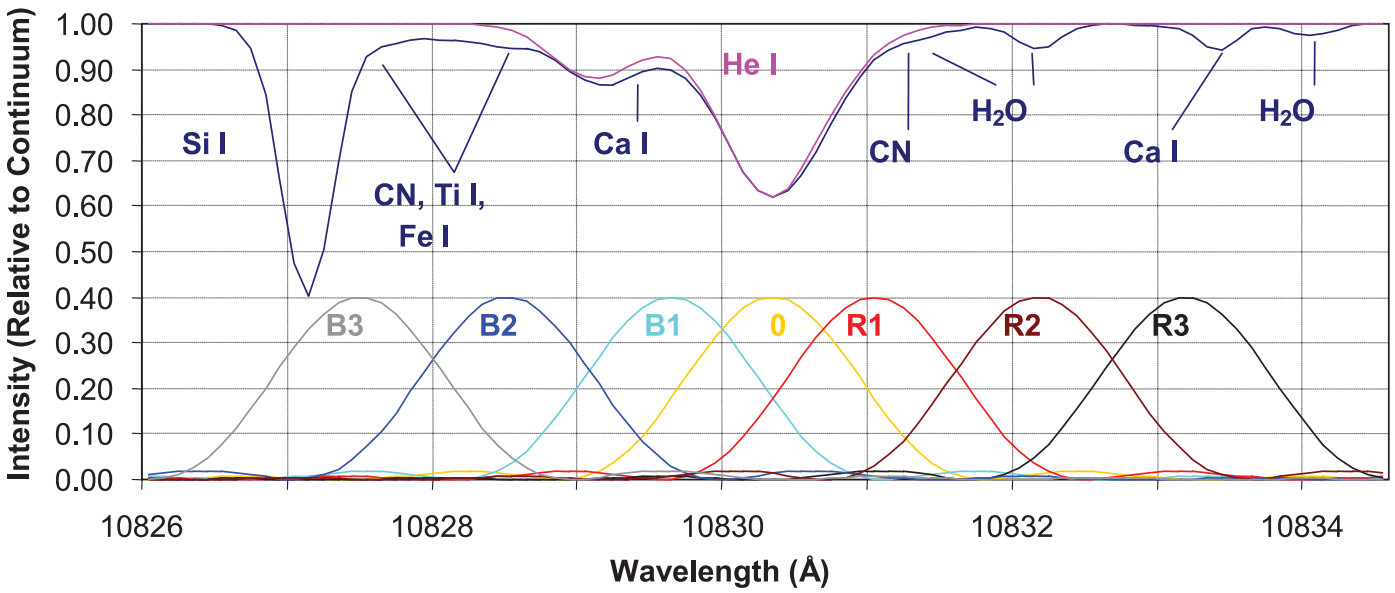

FIG. 12.—Upper curves represent synthetic spectra obtained by fitting the He I 10830 Å line and surrounding solar and terrestrial absorption lines for curve *g* in Fig. 11. The water vapor lines are calculated for a much drier atmosphere than that of Fig. 11. The lower curves represent the CHIP passband for the seven different filter positions that are used in CHIP observations. The scale of the upper curves is normalized to the continuum intensity, while the scale of the lower curves (the CHIP passbands) is arbitrary.

A1. NORMALIZATION PROCEDURE

To correct for limb darkening, we select a set of equally sized boxes in images obtained at each filter position, starting from disk center and moving radially toward the limb (in a swath that only contains quiet-Sun features). We assign a radius and an average brightness of the brightest 20% of the pixels for each of these boxes (the brighter pixels are chosen to eliminate any significant contribution from the He I (λ10830) line), and then fit a limb-darkening function to these results, which provides intensity as a function of radius. The resulting limb-darkening correction is then applied to all pixels that lie within our region of interest (i.e., the location of the filament) for each filter. The corrected filter intensities in our filament region are then represented by I_{jk}(B1), I_{jk}(R1), etc., where *jk* indicates a particular pixel, and $j = 0$, $k = 0$ is the pixel at disk center.

Next, we describe a procedure to remove all of the absorption features shown in Figure 12, other than the helium line. The first step involves finding the continuum intensity by choosing a filter position that has the smallest contribution from photospheric absorption lines, terrestrial water vapor lines, and the He I line. A reasonable spectral region for this measurement is near 10828.5 Å (see Fig. 12), since no water vapor lines exist in this region, and only the shoulders of the Si I line (at 10827.09 Å) and of the minor component (at 10829.07 Å) of the He I line intrude on the region. Since the B2 filter position (at 10828.47 Å) lies in this spectral region, we use it to determine the continuum intensity (the net photospheric absorption for the B2 filter is only about 3%). Note that the B2 filter is also used as the continuum filter in obtaining the line intensity, as described above. Using the mid-blue (B2) filter position, we eliminate effects of He I absorption by choosing a circle centered at disk center in this filter, selecting the brightest 10% of the pixels in that circle, and calculating the average intensity of these pixels. To eliminate the effects of photospheric absorption, we divide this intensity by 0.97 (a factor deduced from synthetic spectra analysis), and this yields the continuum intensity:

$$I_c = I_o(\mathrm{B2})/0.97, \tag{A1}$$

where the "*c*" subscript refers to the continuum, and "*o*" refers to the average intensity of the bright pixels in our central circle.

Once the continuum intensity is established, we determine additive correction factors for photospheric absorption for the outer filters, R2, R3, B2, and B3. We do so by considering a set of horizontal bins of width 0.2 $R_\odot$ across a section of quiet-Sun region in close proximity to our filament, and selecting the brightest 20% of the pixels over the full length of the bin. The bin is then broken vertically into 0.2 $R_\odot$ wide elements, so that we have squares with sides of 0.2 $R_\odot$. The average value of the *previously* selected bright pixels lying within a square is assigned to the center point of the square. Using the B3 filter as an example, the differences Δ_{xy}(B3) are calculated as

$$\Delta_{xy}(\mathrm{B3}) = I_c - I_{xy}(\mathrm{B3}), \tag{A2}$$

where the *xy* subscript refers to the point (x,y) in the center of each square, and I_{xy} refers to the average over the associated square. These differences are subsequently fitted to a function that is odd about $x = 0$ for each value of y (i.e., $y = 0, 0.1, -0.1, 0.2, -0.2, \ldots$), and these functions are used to determine Δ_{jk}(B3), where this last difference applies to each pixel fully on the disk. Hence, the normalized intensity (which should equal the continuum intensity in the absence of He I absorption) is

$$I_{jk}(\mathrm{B3N}) = I_{jk}(\mathrm{B3}) + \Delta_{jk}(\mathrm{B3}). \tag{A3}$$

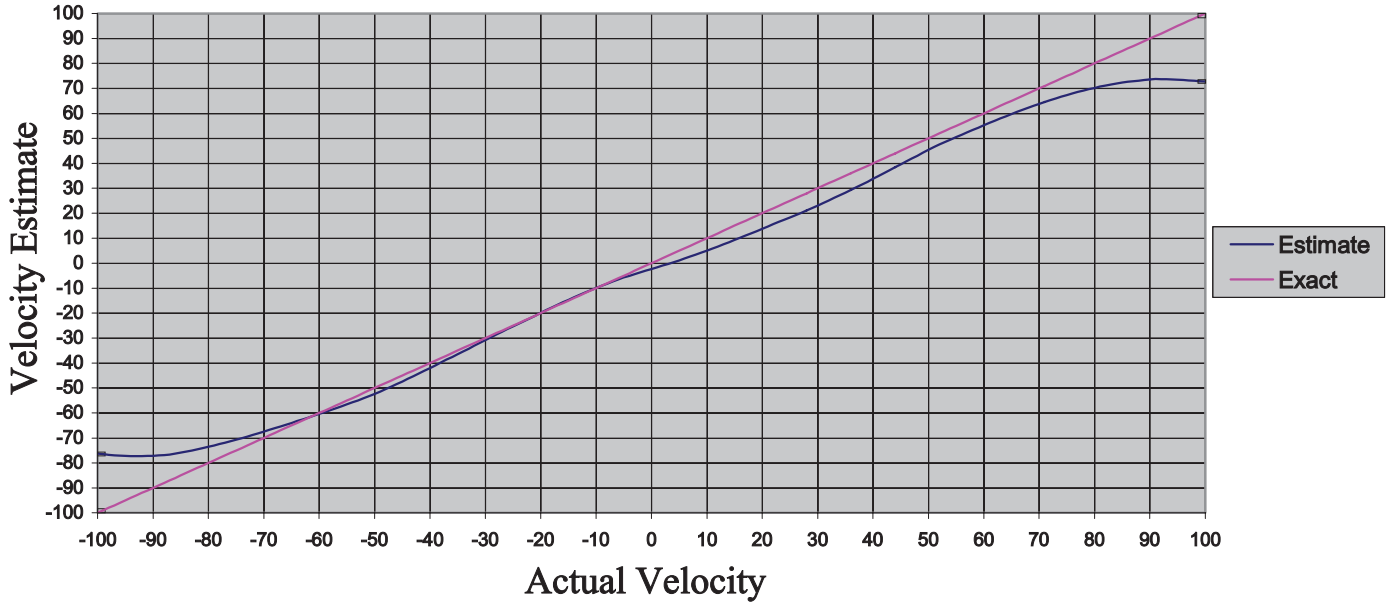

FIG. 13.—Initial line-of-sight velocity (km s^{-1}) estimate for curve *d* using eq. (A7). The perfect (or exact) estimate, where the estimated velocity is the same as the actual velocity, is also shown.

We use this approach on the four outermost filters (B2, B3, R2, R3), but we treat the three inner filters (B1, 0, R1) differently because of the pervasive contamination by the He I line. On the basis of synthetic spectra calculations, the corrections for the presence of photospheric absorption lines and terrestrial water vapor absorption lines is made as follows. We make use of the disk center differences Δ_{00} (B2) and Δ_{00} (R2), and obtain for the filter positions B1, O, and R1

$$\Delta_{jk}(\mathrm{B1}) = 0.8\Delta_{00}(\mathrm{B2}), \qquad \Delta_{jk}(\mathrm{O}) = 0.4\Delta_{00}(\mathrm{B2}) + 0.04\Delta_{00}(\mathrm{R2}), \qquad \Delta_{jk}(\mathrm{R1}) = 0.2\Delta_{00}(\mathrm{B2}) + 0.6\Delta_{00}(\mathrm{R2}). \tag{A4}$$

In general, for filter F, the normalized intensity is written

$$I_{jk}(\mathrm{FN}) = I_{jk}(\mathrm{F}) + \Delta_{jk}(\mathrm{F}). \tag{A5}$$

The intensity of the He I absorption line in the O filter position is given by

$$I_{jk}(\mathrm{O : He\ I}) = I_{jk}(\mathrm{ON}) - I_c.$$

A2. VELOCITY ALGORITHM

Once the normalization procedure is carried out for each of the filter positions, an algorithm can be applied to obtain quantitative line-of-sight velocity information. We turn again to Figure 12, which contains the shape of the CHIP filter passband at each of the seven wavelengths to which the CHIP filter is tuned (*lower curves*). Note that the spacing between the central filter position (O) and the inner blue (B1) and red (R1) filters is less than the spacing between the other filters. This spacing was chosen to provide a more accurate line-of-sight velocity estimate at low speeds, but it has the disadvantage of providing an additional complication in the design of the velocity algorithm. The wavelength scale in Figure 12 can be converted to a velocity scale by noting that a wavelength shift of 0.1 nm corresponds to a velocity shift of 27.7 km s^{-1}.

If the He I 10830 line were Gaussian in shape, and if the CHIP filter positions were all equally spaced, then a reasonable algorithm for determining the line-of-sight velocity would be the intensity-weighted mean wavelength, as determined from the intensities observed at each filter position. Although the above-mentioned criteria are not met, we will use this approach as the foundation for our algorithm. If S_j is the signal strength measured at the jth filter position, then we define the intensity, I_j, at that filter position to be $I_j = 1 - S_j$ for an absorption line (seen against the solar disk). The intensity-weighted mean wavelength is then given by

$$\overline{\lambda} = \frac{\sum_j I_j \lambda_j}{\sum_j I_j}, \tag{A6}$$

where λ_j is the central wavelength of the jth filter position. Since the ratio of the Doppler velocity shift to the speed of light is the same as the ratio of the wavelength shift to the starting wavelength, we obtain the velocity corresponding to equation (A6),

$$V_{\mathrm{initial}} = 3 \times 10^5 \frac{(\overline{\lambda} - \lambda_0)}{\lambda_0} \ \mathrm{km\ s^{-1}}, \tag{A7}$$

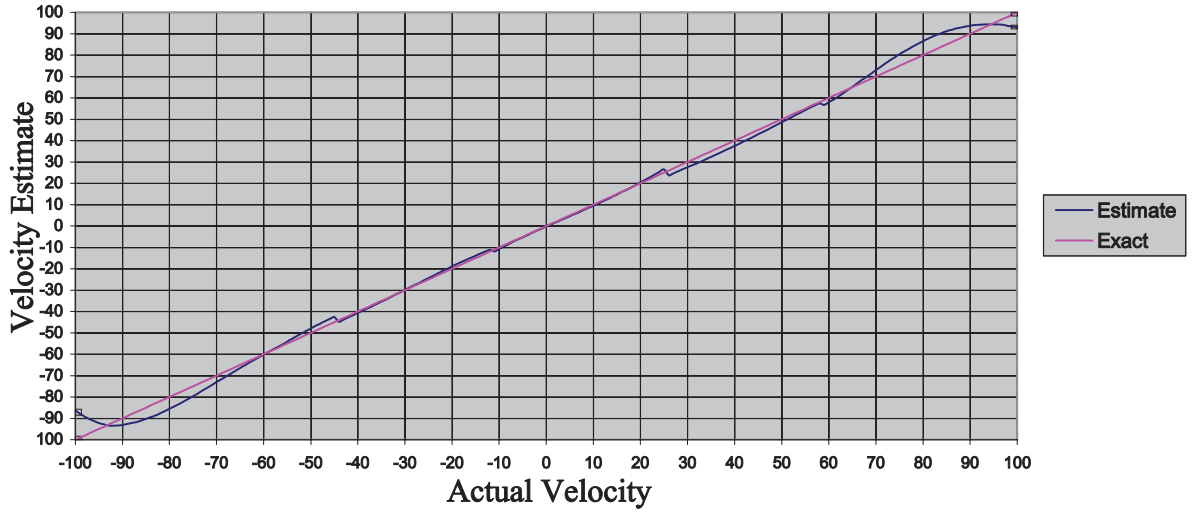

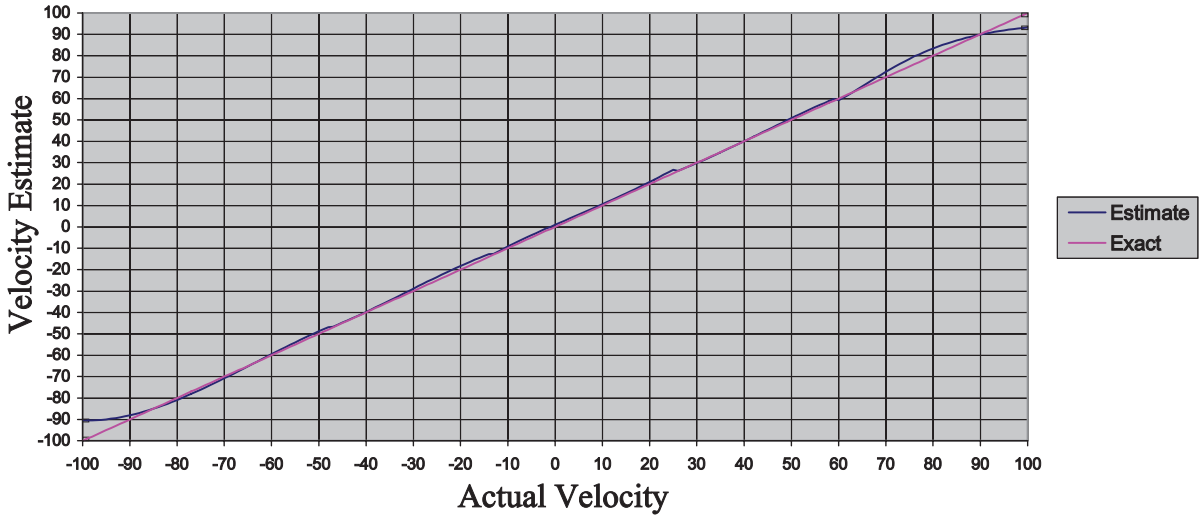

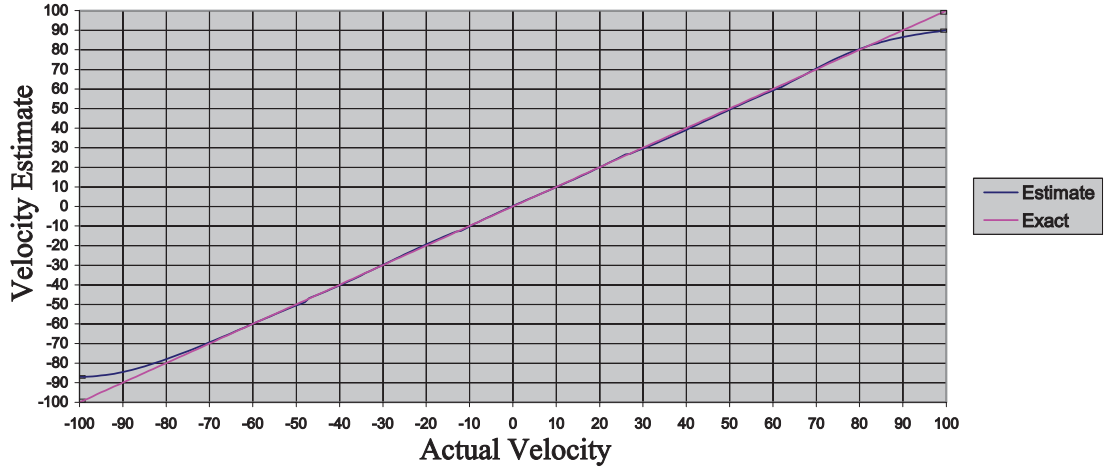

FIG. 14.—Intensity-dependent line-of-sight velocity estimate (using eqs. [A10]–[A12]) applied to (*a*) curve *e*, (*b*) curve *g*, and (*c*) curve *h*. The perfect (or exact) estimate, where the estimated velocity is the same as the actual velocity, is also shown. The units for both axes are km s^{-1}.

where λ_0 is the wavelength of the central filter position (corresponding to the central wavelength of the He I line). By applying the above equation directly to our synthetic spectrum for curve *d* (which is the darkest line with no saturation effects; i.e., it is optically thin), we obtain an initial velocity estimate by shifting our synthetic profile of curve *d* from −100 to 100 km s^{-1}. Using this initial estimate as a base, we determine the corrections that will improve this estimate (this initial estimate is plotted against the actual velocity in Fig. 13). The first correction is a velocity shift by 2.3 km s^{-1}, which leads to a correct estimate when the actual velocity is zero:

$$V_{\rm shift} = \left[3 \times 10^5 \frac{(\overline{\lambda} - \lambda_0)}{\lambda_0} + 2.3\right] \text{ km s}^{-1}. \tag{A8}$$

We use this shifted estimate as a basis for our final set of corrections by considering separately five different ranges of the shifted velocity estimate given above. We denote the correction for the velocity estimate by *C*, and we then specify the form for *C* in each of the five ranges of the shifted velocity estimate:

$$\begin{aligned}
V_{\rm shift} &< -45 \text{ km s}^{-1} & C &= -(V_{\rm shift} + 45)^2/70 \\
-45 \leqslant V_{\rm shift} &< -10 \text{ km s}^{-1} & C &= -1.5 \\
-10 \leqslant V_{\rm shift} &\leqslant 15 \text{ km s}^{-1} & C &= V_{\rm shift}/3 \\
15 < V_{\rm shift} &< 55 \text{ km s}^{-1} & C &= 3.5 \\
V_{\rm shift} &\geq 55 \text{ km s}^{-1} & C &= (V_{\rm shift} + 55)^2/(50 + 3).
\end{aligned} \tag{A9}$$

Our final velocity estimate after applying these corrections is given by

$$V_{\rm final} = V_{\rm shift} + C. \tag{A10}$$

However, this estimated velocity is applicable to the optically thin case, and we require a modified correction that will lead to an estimated velocity more applicable to filaments and plages (i.e., Harvey & Livingston curves *e*, *g*, and *h*). We now modify equation (A9) to obtain a correction factor that is dependent on the intensity of the line for the structure observed, which allows us to take into better account the effect of the growing importance of the blue shoulder with increasing line intensity. The velocity shift in equation (A8) becomes intensity-dependent, and must be replaced by

$$V_{\rm shift} = \left[3 \times 10^5 \frac{(\overline{\lambda} - \lambda_0)}{\lambda_0} + 2 + 2I_{\rm sum}\right] \text{ km s}^{-1}. \tag{A11}$$

Our intensity-dependent correction factor replacing equation (A9) is

$$\begin{aligned}
V_{\rm shift} &< -45 \text{ km s}^{-1} & C &= -(V_{\rm shift} + 45)^2/35 - 5I_{\rm sum} + (0.5/I_{\rm sum}) \\
-45 \leqslant V_{\rm shift} &< -10 \text{ km s}^{-1} & C &= -2.5 + (0.3/I_{\rm sum}) \\
-10 \leqslant V_{\rm shift} &\leqslant 20 \text{ km s}^{-1} & C &= (V_{\rm shift}/3) + 0.5 \\
20 < V_{\rm shift} &< 55 \text{ km s}^{-1} & C &= 6 + I_{\rm sum} - (0.5/I_{\rm sum}) \\
V_{\rm shift} &\geq 55 \text{ km s}^{-1} & C &= (V_{\rm shift} + 55)^{1.5}/4.5 + 8I_{\rm sum}.
\end{aligned} \tag{A12}$$

After plotting the intensity-dependent line-of-sight velocity estimate to the actual velocity for curves *e*, *g*, and *h* (Fig. 14), we find the estimates for curves *g* and *h* to be clearly superior to those for the optically thin case (curve *d*). Yet the velocity estimate for curve *e* is not better than for the optically thin case. Since curves *g* and *h* represent deeper absorption than curve *e*, and our filament of interest in the present study is significantly dark in the observations, we use the corrections listed in equation (A12) to obtain an intensity-dependent line-of-sight velocity estimate instead of the optically thin corrections listed in equation (A9). Based on Figures 14*b* and 14*c*, we conclude our filament velocity estimates are good between −90 and +90 km s^{-1}, with an uncertainty of ±5 km s^{-1}.

REFERENCES

Antiochos, S. K., MacNeice, P. J., & Spicer, D. S. 2000, ApJ, 536, 494
Athay, R. G., & Moreton, G. E. 1961, ApJ, 133, 935
Balasubramaniam, K. S., Pevtsov, A. A., & Neidig, D. F. 2007, ApJ, 658, 1372
Chen, P. F., Fang, C., & Shibata, K. 2005, ApJ, 622, 1202
Elmore, D. F., et al. 1998, Appl. Opt., 37, 4270
Engvold, O. 2001, Solar Prominence Fine Structures, in Encyclopedia of Astronomy and Astrophysics, ed. P. Murdin (London: Nature)
Eto, S., et al. 2002, PASJ, 54, 481
Gilbert, H. R., Falco, L. E., Holzer, T. E., & MacQueen, R. M. 2006, ApJ, 641, 606
Gilbert, H. R., & Holzer, T. E. 2004a, ApJ, 610, 572
Gilbert, H. R., Holzer, T. E., Thompson, B. J., & Burkepile, J. T. 2004b, ApJ, 607, 540
Harvey, J. 1969, PhD thesis, Univ. of Colorado
Hyder, C. L. 1966, Z. Astrophys., 63, 78
Isobe, H., & Tripathi, D. 2006, A&A, 449, L17
Isobe, H., Tripathi, D., Asai, A., & Jain, R. 2007, Sol. Phys., 246, 89
Jing, J., Lee, J., Spirock, T. J., Xu, Y., Wang, H., & Choe, G. S. 2003, ApJ, 584, L103
Khan, J. I., & Aurass, H. 2002, A&A, 383, 1018
Kleczek, J., & Kuperus, M. 1969, Sol. Phys., 6, 72
Lin, R. P., et al. 2002, Sol. Phys., 210, 3
Low, B. C. 1996, Sol. Phys., 167, 217
Metcalf, T. R., Hudson, H. S., Kosugi, T., Puetter, R. C., & Pina, R. K. 1996, ApJ, 466, 585
Moreton, G. E. 1960, AJ, 65, 494
Ofman, L., & Thompson, B. J. 2002, ApJ, 574, 440
Okamoto, T. J., Nakai, H., Keiyama, A., Narukage, N., UeNo, S., Kitai, R., Kurokawa, H., & Shibata, K. 2004, ApJ, 608, 1124

Oliver, R., & Ballester, J. L. 2002, Sol. Phys., 206, 45
Oliver, R., Ballester, J. L., Hood, A. W., & Priest, E. R. 1992, ApJ, 400, 369
———. 1993, ApJ, 409, 809
Pohjolainen, S., et al. 2001, ApJ, 556, 421
Ramsey, H. E., & Smith, S. F. 1965, AJ, 70, 688
———. 1966, AJ, 71, 197
Smith, S. F., & Harvey, K. L. 1971, in Physics of the Solar Corona, ed. C. J. Macris et al. (Dordrecht: Reidel), 156
Terradas, J., Molowny-Horas, R., Wiehr, E., Balthasar, H., Oliver, R., & Ballester, J. L. 2002, A&A, 393, 637
Terradas, J., Oliver, R., & Ballester, J. L. 2001, A&A, 378, 635
Thompson, B. J., Plunkett, S. P., Gurman, J. B., Newmark, J. S., St. Cyr, O. C., Michels, D. J., & Delaboudinière, J.-P. 1998, Geophys. Res. Lett., 25, 2461
Thompson, B. J., et al. 1999, ApJ, 517, L151
———. 2000, Sol. Phys., 193, 161
Tripathi, D., & Raouafi, N.-E. 2007, A&A, 473, 951
Uchida, Y. 1968, Sol. Phys., 4, 30
———. 1970, PASJ, 22, 341
Vršnak, B. 1984, Sol. Phys., 94, 289
———. 1990, Sol. Phys., 129, 295
Vršnak, B., Veronig, A. M., Thalmann, J. K., & Žic, T. 2007, A&A, 471, 295
Vršnak, B., Warmuth, A., Brajsa, R., & Hanslmeier, A. 2002, A&A, 394, 299
Warmuth, A., Vršnak, B., Aurass, H., & Hanslmeier, A. 2001, ApJ, 560, L105